

Third-order nonlinear influence on the specular reflectivity of two-dimensional waveguide-based photonic crystals

M. G. Banaee, A. R. Cowan, and Jeff F. Young

Department of Physics and Astronomy, Advanced Materials and Process Engineering Laboratory

The University of British Columbia, Vancouver, British Columbia, V6T 1Z4

Abstract

Specular reflectivity spectra of plane waves incident on two-dimensional waveguide-based photonic crystals are rigorously calculated using the linear and third order nonlinear susceptibilities of the semiconductor core layer. The Fano-like features associated with coupling to leaky photonic eigenstates 'attached' to the porous slab shift and distort at high intensities. While some of this nonlinear behaviour is qualitatively similar to that observed in simple Fabry-Perot cavities, there are striking differences. The main difference is that the Q values and in-plane dispersion of the microcavity modes associated with the leaky eigenstates of the photonic crystal can be engineered over a wide range by varying the properties of the etched texture. Examples are given that demonstrate bistable behaviour, and intensity-dependent reflectivities that can vary from zero to unity. Both degenerate (single beam) and non-degenerate (pump and signal beam) cases are considered.

1. INTRODUCTION

It is well-established that planar semiconductor waveguides penetrated by two dimensional (2D) periodic arrays of deeply etched holes exhibit many of the interesting and potentially useful properties of bulk 2D photonic crystals¹⁻⁸. In particular, it is possible to open optical "bandgaps" for modes localized to these porous waveguides, and the 2D dispersion of prop-

agating modes outside of the bandgaps can be tailored over a wide range. Linear and point defect states with energies inside the bandgaps act like waveguides and sub-wavelength microcavities respectively^{9,10}. Much effort is now being devoted to reducing the losses of these defect states in crystals with sub-micron hole spacing, that operate in the near infrared.

The extreme linear optical properties of 2D planar photonic crystals (2DPPC) make them an attractive platform upon which to fully integrate various optical information processing functions that are currently implemented using discrete components. The strong optical confinement in this high-index-contrast geometry may also facilitate practical nonlinear optical processes at lower power levels than those required using other geometries.

We recently reported a calculation that suggests the second harmonic conversion efficiency of a plane wave incident on the top surface of a strongly-textured 2DPPC can be enhanced by several orders of magnitude over that obtained from an untextured waveguide when both the incident and second harmonic fields inside the 2DPPC are resonant with photonic crystal eigenstates¹¹. The leaky eigenstates of photonic crystal waveguides are in some senses similar to 1D Fabry-Perot cavity modes, but there are important differences: the confinement is provided by total internal reflection of evanescent Fourier components of the field in the waveguide, and the Q is determined by grating coupling of these evanescent components to radiation modes. In the 1D Fabry Perot, the mirrors around the cavity are *needed* to establish a well defined mode, and they actually *reduce* the direct coupling of radiation modes to the cavity region. In contrast, the grating on a textured waveguide actually *spoils* the otherwise infinite Q of pure slab modes, but it is *needed* to allow coupling between the cavity and the radiation modes. To our knowledge, the microcavity nature of weak, 1D-textured waveguides was first related to enhanced optical nonlinearities by Neviere et al.^{12,13}

The third order response of Fabry-Perot cavities, 1D-textured waveguides and bulk photonic crystals has received considerable attention. It is well established that optical limiting and bistability can be observed in these systems when the cavity possesses a sizable $\chi^{(3)}$ ¹³⁻¹⁹. The influence of Kerr nonlinearities on the bandstructure of bulk photonic crystals has also

been considered theoretically^{20,21} and experimentally observed in 1D silicon crystals using free-carrier effects²².

In comparison to 1D Fabry-Perot cavities, textured waveguides offer a relatively easy means by which to angle-tune the cavity finesse or Q , while simultaneously introducing a much richer in-plane dispersion for the microcavity modes. Two dimensional, high-index-contrast texture offers even more flexibility and richness than 1D surface gratings. The purpose of the present paper is to quantify the microcavity-enhanced third order response of 2D-textured GaAs waveguides in which the etched holes completely penetrate the waveguide core.

The linear dispersion and quality factors of leaky modes attached to these structures have recently been studied both theoretically and experimentally.⁵⁻⁸ While 1D *surface* gratings merely probe the dispersion of the underlying waveguide, strong 2D texture establishes a rich bandstructure characterized by relatively large gaps, and weakly dispersive bands. In a 2D square lattice, symmetry dictates that the bands at zone centre are either doubly or singly degenerate. At zone centre, doubly degenerate bands have finite Q values, while non-degenerate bands acquire an infinite Q . The Q values of nondegenerate bands therefore vary abruptly near zone centre. Some bands can also acquire infinite Q values away from zone centre, in the vicinity of anticrossings. Anticrossings can occur between bands of the same polarization at any point in the Brillouin zone. Thus microcavity modes with arbitrarily large Q values can theoretically be coupled to at any incident angle and with any polarization in 2DPPC structures. These arguments strictly apply only to infinite sized 2DPPCs. The finite size of the excitation spot and/or the textured area of the waveguide will fundamentally limit the maximum achievable Q in particular experiments. Manufacturing imperfections will also limit the maximum attainable Q .

While high Q modes offer the strongest field enhancements, some applications are sensitive to bandwidth, which is restricted in high Q cavities. High-index-contrast texture can be used to tune Q values over a much wider range than in waveguides textured only on the surface. Waveguides textured with high-index-contrast 2D gratings therefore offer a num-

ber of bands with different polarizations, each with angle-dependent Q values that can be engineered over a wide range.

2. THEORY

Fig.(1) is a schematic diagram of the waveguide photonic crystal structure that we consider here. It consists of a thin GaAs slab of thickness w penetrated completely by a square array of circular holes on a pitch Λ , with radius r . The bottom of the GaAs is separated from the GaAs substrate by a uniform layer of dielectric (wet-oxidized $\text{Al}_{0.98}\text{Ga}_{0.02}\text{As}$) of thickness d . Similar structures have been fabricated and the dispersion of the lowest 5 leaky bands has been measured using angle-resolved, broadband specular reflectivity spectroscopy⁷. The specular reflectivity spectra exhibit Fano-shaped resonances when the frequency and in-plane momentum of the incident radiation matches that of a leaky photonic crystal mode. The width of the Fano resonances is inversely related to the Q of the corresponding microcavity modes. Both the dispersion and Q values of the bands agree well with the dispersion obtained by calculating the specular reflectivity spectra from these porous waveguides using a Green's function formula described in detail elsewhere⁸.

Very briefly, the Green's function formalism described in Ref. [8] relies on the fact that the textured GaAs membrane is thin compared to the wavelengths of radiation associated with the lower lying leaky bands. Using an integral formulation of the Maxwell equations Fourier transformed in the x-y plane, the problem essentially reduces to self-consistently solving for the 2D Fourier components of the total electric field excited in the textured grating, assuming the fields do not vary across the thickness of the grating. In a square grating the 2D reciprocal lattice vectors are simply given by $\vec{\beta}_n = \beta_g(i\hat{x} + j\hat{y})$ where $\beta_g = 2\pi/\Lambda$ and i and j are integers. By truncating the total number of Fourier components considered, the problem is reduced to an algebraic matrix equation driven by an externally-generated plane wave incident at a well-defined frequency, ω and in-plane wavevector, $\vec{\beta}_{inc}$. The self-consistent equation that couples each field component in the grating layer is then,

$$\vec{E}(\omega : \vec{\beta}_{inc} + \vec{\beta}_n) = \vec{E}^{hom}(\omega : \vec{\beta}_{inc} + \vec{\beta}_n) + \vec{G}(\omega : \vec{\beta}_{inc} + \vec{\beta}_n) \Delta \vec{P}(\omega : \vec{\beta}_{inc} + \vec{\beta}_n), \quad (1)$$

where

$$\Delta \vec{P}(\omega : \vec{\beta}_{inc} + \vec{\beta}_n) = \Delta \chi^{(1)}(-\omega; \omega : \vec{\beta}_n - \vec{\beta}_m) \vec{E}(\omega : \vec{\beta}_{inc} + \vec{\beta}_m), \quad (2)$$

is the polarization due to the *difference* in the actual susceptibility from that of an untextured waveguide with the same dimensions, $\Delta \chi^{(1)}(-\omega; \omega)$. Repeated reciprocal lattice wavevectors are implicitly summed over throughout. The driving term, $\vec{E}^{hom}(\omega : \vec{\beta}_{inc} + \vec{\beta}_n)$, is the field in the grating layer that would be excited by the external plane wave if there was no texture in the multilayer structure. It is nonzero only for $\vec{\beta}_n = 0$. Once all of the $\vec{E}(\omega : \vec{\beta}_{inc} + \vec{\beta}_n)$ are determined in the grating, another Greens function propagates the $\vec{\beta}_{inc}$ component of the polarization into the upper half space where it is added to the specular reflection of the incident plane wave from the untextured multilayer to obtain the total reflectivity. Explicit expressions for both Green's functions can be found in Ref.[8].

For illustrative purposes we choose a thin GaAs slab supported by an alumina cladding and penetrated by a square lattice of through-holes. The structure is described by parameters $\Lambda = 500nm$, $r = 164nm$, $d = 1.8\mu m$, $w = 80nm$, $\epsilon = 2.56$ for the oxide cladding layer, and a fully-dispersive GaAs core layer. A typical reflectivity spectrum (specular reflectivity) excited by a plane wave with in-plane wave vector $\beta_{//} = 0.01\beta_g$ oriented along the X direction of the square Brillouin zone is shown in Fig.(2). The three features in the s-polarized spectrum and the single feature in the p-polarized spectrum that go to unity reflectivity are signatures of coupling of the incident plane wave to leaky photonic crystal eigenstates localized in the vicinity of the textured membrane. Similar plots for a range of incident wavevectors faithfully reproduce experimentally measured reflectivity spectra from this type of sample⁷. Fig.(3) shows the dispersion of these 3 s-polarized, and the one p-polarized band away from zone centre, along the X direction of the Brillouin zone. These are the four lowest energy bands at zone centre, and the corresponding eigenstates are principally composed of

different linear combinations of fields with wavevectors close to the four smallest reciprocal lattice vectors that describe the square, periodic texture. Fig.(4) shows real space plots of the electric field magnitude within the unit cell for each of the four modes indicated in the reflectivity spectrum of Fig.(2). The high-energy band is largely in the air holes, the low energy band is largely in the dielectric, and the two intermediate energy bands are more uniformly distributed within the unit cell.

Our principal interest in the present paper is to study the influence on the specular reflectivity of the nonzero third order susceptibility in the GaAs slab. The effect is largest when strong fields are developed inside the slab. For a fixed incident field magnitude, the strength of the fields generated within the textured slab will be largest when the leaky eigenmodes are excited, the internal field enhancement then being related to the Q (inverse linewidth) of the specific resonance. Fig.(5) plots the inverse Q of each of the four bands shown in Fig.(3). As described in detail elsewhere⁵, symmetry considerations dictate that the two bands that are non-degenerate at zone centre must have infinite Q values there. The bands that are degenerate at zone centre have finite Q values. For this particular structure, the largest third order effects are therefore expected to occur near zone-centre when exciting the first and fourth bands. These happen to be the most dispersive bands for this particular filling fraction of the square crystal structure. For other filling fractions the ordering of the degenerate and nondegenerate bands is different, but it is always the first and fourth bands that exhibit the most dispersion along the X direction. These 2D textured waveguides therefore offer considerable flexibility for engineering the energies and dispersion of modes that are particularly responsive to the third order effects illustrated below.

Starting with the degenerate (single strong pump field) case, the total polarization in the grating can be expressed as:

$$\Delta\vec{P}(\omega : \vec{\beta}_{inc} + \vec{\beta}_n) = \Delta\vec{\chi}^{(1)}(-\omega; \omega : \vec{\beta}_n - \vec{\beta}_k)\vec{E}(\omega : \vec{\beta}_{inc} + \vec{\beta}_k) +$$

$$\vec{\chi}^{(3)}(-\omega; \omega, -\omega, \omega : \vec{\beta}_n - \vec{\beta}_m + \vec{\beta}_l - \vec{\beta}_k) \times$$

$$\vec{E}(\omega : \vec{\beta}_{inc} + \vec{\beta}_m) \vec{E}^*(\omega : -\vec{\beta}_{inc} - \vec{\beta}_l) \vec{E}(\omega : \vec{\beta}_{inc} + \vec{\beta}_k) \quad (3)$$

or, explicitly in terms of Cartesian components, and suppressing the frequency argument and the implied momentum convolutions,

$$\Delta P_\mu = \Delta \chi_{\mu\gamma}^{(1)} E_\gamma + \chi_{\mu\alpha\delta\gamma}^{(3)} E_\alpha E_\delta^* E_\gamma, \quad (4)$$

Using the same notation, Eq.(4) can be written as:

$$\Delta P_\mu = (\Delta \chi_{\mu\gamma}^{(1)} + \theta_{\mu\gamma}^{(3)}) E_\gamma = \chi_{\mu\gamma}^{eff} E_\gamma, \quad (5)$$

where explicitly

$$\begin{aligned} \theta_{\mu\gamma}^{(3)}(\omega : \vec{\beta}_n - \vec{\beta}_k) &= \chi_{\mu\alpha\delta\gamma}^{(3)}(-\omega; \omega, -\omega, \omega : \vec{\beta}_n - \vec{\beta}_m + \vec{\beta}_l - \vec{\beta}_k) \times \\ &E_\alpha(\omega : \vec{\beta}_{inc} + \vec{\beta}_m) E_\delta^*(-\vec{\beta}_{inc} - \vec{\beta}_l), \end{aligned} \quad (6)$$

and

$$\chi_{\mu\gamma}^{eff} = \Delta \chi_{\mu\gamma}^{(1)} + \theta_{\mu\gamma}^{(3)} = \Delta \chi_{\mu\gamma}^{(1)} + \chi_{\mu\alpha\delta\gamma}^{(3)} E_\alpha E_\delta^*, \quad (7)$$

where the momentum convolutions and frequencies are again implied. Eq.(7) is simply the usual “intensity dependent refractive index” associated with $\chi^{(3)}$ processes, generalized to this textured geometry.

Finally, the field inside of the grating is:

$$\begin{aligned} E_\alpha(\omega : \vec{\beta}_{inc} + \vec{\beta}_n) &= E_\alpha^{hom}(\omega : \vec{\beta}_{inc} + \vec{\beta}_n) + G_{\alpha\mu}(\omega : \vec{\beta}_{inc} + \vec{\beta}_n) \times \\ &\chi_{\mu\gamma}^{eff}(\vec{\beta}_n - \vec{\beta}_k) E_\gamma(\omega : \vec{\beta}_{inc} + \vec{\beta}_k), \end{aligned} \quad (8)$$

The solution of Eq. (8) is obtained by iteratively determining the field on the left hand side using a running average of previously calculated fields to estimate χ^{eff} , through Eq. (7), until convergence is obtained.

Here we assume that the matrix elements of the $\theta^{(3)}$ tensor are determined by the symmetry of the bulk material in which the 2D grating is etched. For $\bar{4}3m$ (GaAs) and $m\bar{3}m$ (Si, Ge) group symmetry, the only nonzero elements of the $\chi^{(3)}$ tensor can be categorized in four groups²³:

$$\begin{aligned}\chi_{xxxx}^{(3)} &= \chi_{yyyy}^{(3)} = \chi_{zzzz}^{(3)}, \\ \chi_{xxyy}^{(3)} &= \chi_{xxzz}^{(3)} = \chi_{yyxx}^{(3)} = \chi_{yyzz}^{(3)} = \chi_{zzxx}^{(3)} = \chi_{zzyy}^{(3)}, \\ \chi_{xyxy}^{(3)} &= \chi_{xzzx}^{(3)} = \chi_{yxyx}^{(3)} = \chi_{yzyz}^{(3)} = \chi_{zyyz}^{(3)} = \chi_{zxzx}^{(3)}, \\ \chi_{xyyx}^{(3)} &= \chi_{xzzx}^{(3)} = \chi_{yxyx}^{(3)} = \chi_{yzyz}^{(3)} = \chi_{zyyz}^{(3)} = \chi_{zxzx}^{(3)}.\end{aligned}\tag{9}$$

where the subscripts refer to the principal crystal axes. The diagonal elements are taken to be $-9.74 \times 10^{-11} esu^{24}$ from experimental measurements on GaAs. We are unaware of measured values for the off diagonal elements and assume here that they are equal to the diagonal components. The formalism allows the principal photonic crystal axes to be arbitrarily oriented with respect to the principal crystal axes, but all results reported here have them aligned. To take into account different numbers of identical terms that contribute to the total nonlinear polarization, these $\chi_{i,j,k,l}^{(3)}$ are multiplied by 3/4 for this degenerate calculation, and by 3/2 for the nondegenerate case discussed next.

3. RESPONSE WITH TWO DIFFERENT FREQUENCIES

We now consider the nondegenerate situation where a relatively strong pump beam with frequency ω_p and in-plane wavevector $\vec{\beta}_{pump}$, induces changes in the bandstructure that are monitored by a relatively weak probe beam with (variable) frequency ω_s and in-plane wavevector $\vec{\beta}_{probe}$. When the pump beam is much stronger than the probe, Eq. (8) can be used to solve for all of the field components at the pump frequency, independent of the probe.

The reflectivity of the signal beam, including the refractive index changes induced by the pump beam, can then be obtained using,

$$\begin{aligned}
E_\alpha(\omega_s, \vec{\beta}_{probe} + \vec{\beta}_n) &= E_\alpha^{hom}(\omega_s, \vec{\beta}_{probe} + \vec{\beta}_n) + G_{\alpha\mu}(\omega_s, \vec{\beta}_{probe} + \vec{\beta}_n) \times \\
&[\Delta\chi_{\mu\gamma}^{(1)}(-\omega_s; \omega_s : \vec{\beta}_n - \vec{\beta}_k) E_\gamma(\omega_s : \vec{\beta}_{probe} + \vec{\beta}_k) + \\
&\chi_{\mu\alpha\delta\gamma}^{(3)}(-\omega_s; \omega_p, -\omega_p, \omega_s : \vec{\beta}_n - \vec{\beta}_m + \vec{\beta}_l - \vec{\beta}_k) \times \\
&E_\alpha(\omega_p : \vec{\beta}_{pump} + \vec{\beta}_m) E_\delta^*(\omega_p : -\vec{\beta}_{pump} - \vec{\beta}_l) \times \\
&E_\gamma(\omega_s : \vec{\beta}_{probe} + \vec{\beta}_k)], \tag{10}
\end{aligned}$$

Note that Eq.(10) is of the same form as Eq. (5), but with

$$\chi_{\mu\gamma}^{eff} = \Delta\chi_{\mu\gamma}^{(1)}(-\omega_s; \omega_s) + \chi_{\mu\alpha\delta\gamma}^{(3)}(-\omega_s; \omega_p, -\omega_p, \omega_s) E_\alpha(\omega_p) E_\delta^*(\omega_p), \tag{11}$$

The solution for the nondegenerate problem thus consists of first solving the degenerate problem iteratively at ω_p , and using the fields so generated to evaluate the nonlinear contribution to χ^{eff} . For simplicity, and for lack of any data on the frequency dependence of $\chi^{(3)}$ near degeneracy, $\chi^{(3)}$ is assumed not to depend on ω_s . The reflectivity at each ω_s is thus obtained in a single iteration.

4. RESULTS

Fig.(6) shows the reflectivity near the highest energy s polarized mode, s3, at an in-plane wavevector of $\vec{\beta}_{//} = 0.01\beta_g\hat{x}$, for four different incident intensities. This mode has a Q of ~ 2900 . The blue shift of the peak with increasing incident intensity is consistent with the negative value of $\chi^{(3)}$ in the GaAs slab. The lineshape becomes increasingly asymmetric as the high energy edge sharpens at higher power. This is indicative of positive feedback that can ultimately lead to multi-valued solutions and bistability, as discussed below. As

the frequency decreases towards the peak of the nominal mode, the internal field strength builds and pulls the effective, renormalized mode energy towards the incident frequency. This, self-consistently, further increases the internal field strength since the incident field is now ‘closer’ to the renormalized mode frequency. In contrast, on the low energy side, the reflectivity is smoothly varying because decreasing energy below the renormalized mode energy decreases the field enhancement, which allows the renormalized mode to smoothly shift back to its nominal position. Our structure was chosen so that this mode occurs at a minimum of the background Fabry-Perot (1D) oscillations associated with the thick oxide layer. This gives the reflectivity feature a nearly Lorentzian shape. From Fig.(6) it is clear that the reflectivity near 10744.5 cm^{-1} varies from ~ 0.25 at low power, to unity at an incident power of $\sim 3800 \text{ kW/cm}^2$.

Fig.(7) illustrates the effect of χ^3 on the reflectivity spectrum associated with the lowest energy s-polarized mode, s1, at the same in-plane wavevector. At low powers, the linear reflectivity spectrum associated with s1 is far from Lorentzian because it occurs near a peak in the background, ‘1D’ Fabry-Perot reflectivity. This has a considerable effect on the lineshape at higher powers: it blue shifts and develops a slight asymmetry at very low intensities, but as soon as the shift becomes comparable to the linewidth, it rapidly washes out. This represents a significant *qualitative* difference in the nonlinear response of waveguide-based photonic crystal microcavities in comparison to Fabry-Perot cavities. A detailed analysis will be reported elsewhere, but the reason for this different behaviour has to do with the relative phases of the zeroth order and higher order polarization components associated with each leaky mode. This relative phase is responsible for the Fano- rather than Lorentzian lineshapes in the linear spectra, and for the ‘unusual’ nonlinear response of these lineshapes. *Quantitatively*, these effects occur at much lower incident intensities than was the case for mode s3. This is directly attributable to the relatively high Q ($\sim 12,000$) of s1, which allows a much larger buildup of the internal field strength. The factor of ~ 4 increase in Q reduces the intensity needed to obtain the same fractional shift, $\Delta\omega \sim \omega_0/Q$ by a factor of ~ 30 . For mode s1, the reflectivity can be changed from 0% to $\sim 80\%$ near

9679 cm^{-1} by increasing the power to $\sim 150 kW/cm^2$.

At higher incident powers than considered so far, the reflectivity spectra can develop step-discontinuities on the high frequency side of the features. This suggests the possibility of bistable behaviour at a fixed frequency as a function of the input power. Fig. (8) illustrates this in the case of mode s3. In Fig.(8) the solid curve is the calculated reflectivity at 10745.5 cm^{-1} as the power is increased, and the dashed line is the corresponding curve when the power is decreased from its peak value of $\sim 7000 kW/cm^2$. For the Fano-shaped s1 feature, bistable behaviour is not observed until the lineshape is grossly distorted and that point the hysteresis loop is very small.

Although not shown, qualitatively similar behaviour is observed when exciting the flat, nearly degenerate s and p polarized bands, but the corresponding power levels are much higher due to the low Q values of these modes ($Q \sim 50$).

To this point we have only considered the degenerate situation where a single strong pump beam is used to excite the sample. All reflectivities have thus been self-consistently determined by the iterative procedure described above. Another possibly useful scenario is where a strong pump is used to excite a leaky mode at a fixed frequency, ω_p , and thus modify the effective dielectric constant of the slab as experienced by a weak probe beam incident at any frequency, ω_s in the vicinity of these four bands. Fig.(9) shows the calculated reflectivity of the weak probe beam in the vicinity of the s1 resonance when the sample is excited near the highest energy s-polarized resonance, at 10744 cm^{-1} , with different intensities. Under these nondegenerate conditions the Fano lineshape remains as the feature shifts to higher energies with increasing intensity. Here a pump beam at 10744 cm^{-1} with an intensity of $\sim 3000 kW/cm^2$ could be used to change the reflectivity of a weak probe beam at $\sim 9679 cm^{-1}$ from zero to unity. Comparing this to the influence of the same pump beam on the probe spectrum near s3, as shown in Fig.(10), we note that the effect is weaker. That is, the strong pump influences the linear lineshape of the mode it is exciting more than it influences a more remote mode. This can be qualitatively understood easily with reference to the real space mode profiles shown in Fig. 4. There is very little mode overlap of s1 and s3, hence

the nonlinear change in effective index induced by the pump is largely irrelevant to the other mode.

This brings up an important issue. The $\chi^{(3)}$ considered here is an intrinsic nonlinearity characteristic of bound electrons in GaAs. If a free-carrier-related nonlinearity was considered, as in the experiments reported in Ref.[22], then the calculation would have to be altered in several ways. First, the absolute magnitude of the $\chi^{(3)}$ elements would change and become proportional to the local free carrier density. The symmetry of the tensor would also change to reflect the effective mass tensor of the free carriers, and finally, a transport equation would have to be independently solved to determine the distribution of carriers excited in the unit cell. This is well beyond the scope of the present paper.

5. CONCLUSIONS

We have extended a proven Green's function formalism for accurately describing the photonic eigenstates of 2D photonic crystal waveguides with strong index contrast to include the intrinsic third order nonlinear response of the GaAs waveguide slab material. Using an iterative numerical solver we have calculated the way in which the specular reflectivity spectrum in the vicinity of leaky photonic crystal modes depends on the incident intensity of a single pump beam. Strong asymmetric lineshapes are found, and beyond critical intensities that depend on the Q of the associated leaky modes, bistable behaviour is observed. The influence of a strong pump beam at a fixed frequency near one mode on the specular reflectivity of a weak probe beam was also considered. In both cases, the potential for achieving large, intensity-dependent changes in the reflectivity are demonstrated. Such properties may be useful in all-optical applications such as power-limiting and light-by-light switching.

Quite generally, these phenomena can be interpreted as nonlinear microcavity enhancement effects associated with the leaky photonic crystal eigenstates 'attached' to the porous waveguide structure. While similar effects can and have been observed in nonlinear Fabry-Perot cavities and in waveguides textured with shallow 1D gratings, we have demonstrated

the richness in behaviour that can be observed in these 2D, strongly-modulated structures. By varying the air filling-fraction, the thickness of the oxide cladding, and the in-plane wavevector, the energies, Q values and spatial overlaps of the pump and probe microcavity modes can be varied over wide ranges.

6. Acknowledgements

We would like to acknowledge the financial support of Galian Photonics Inc., the Natural Sciences and Engineering Research Council, and the Canadian Institute for Advanced Research. We would also like to acknowledge very useful discussions with Mr. Paul Barclay.

REFERENCES

1. Jeff F. Young, P. Paddon, V. Pacradouni, T. Tiedje, and S. Johnson, "Photonic Lattices in Semiconductor Waveguides", *Future Trends in Microelectronics*, S. Luryi, J. Xu, and A. Zaslavsky Eds. (John Wiley & Sons, Inc., Toronto, 1999) pp 423-432.
2. M. Kanskar, P. Paddon, V. Pacradouni, R. Morin, A. Busch, J. F. Young, S. R. Johnson, J. Mackenzie, and T. Tiedje, "Observation of leaky slab modes in air-bridge semiconductor waveguides with a two-dimensional photonic lattice", *Appl. Phys. Lett.* **70**, 1438-1440 (1997).
3. D. M. Atkin, P. S. J. Russell, T. A. Birks, and P. J. Roberts, "Photonic band structure of guided Bloch modes in high index films fully etched through with periodic microstructure", *J. Mod. Opt.* **43**, 1035-1053 (1996).
4. Steven G. Johnson, Shanhui Fan, Pierre R. Villeneuve, J.D. Joannopoulos, and L.A. Kolodziejski, "Guided modes in photonic crystal slabs", *Phys. Rev. B* **60**, 5751-5758 (1999).
5. P. Paddon and Jeff F. Young, "Two-dimensional vector-coupled-mode theory for textured planar waveguides", *Phys. Rev. B* **61**, 2090-2101 (2000).
6. V. N. Astratov, D. M. Whittaker, I. S. Culshaw, R. M. Stevenson, M. S. Skolnick, T. F. Krauss, and R. M. De La Rue, "Photonic band-structure effects in the reflectivity of periodically patterned waveguides", *Phys. Rev. B* **60**, R16255-R16258 (1999).
7. V. Pacradouni, J. Mandeville, A. R. Cowan, P. Paddon, and Jeff F. Young, "Photonic Bandstructure of Dielectric Membranes Periodically Textured in Two Dimensions", *Phys. Rev. B* **62**, 4204-4207 (2000).
8. A.R. Cowan, P. Paddon, V. Pacradouni, and Jeff F. Young, "Resonant scattering and mode coupling in two-dimensional textured planar waveguides", *J. Opt. Soc. Am. A* **18**, 1160-1171 (2001).

9. Steven G. Johnson, Pierre R. Villeneuve, Shanhui Fan, and J.D. Joannopoulos, "Linear waveguides in photonic-crystal slabs", *Phys. Rev. B* **62**, 8212-8222 (2000).
10. O. Painter, R. K. Lee, A. Scherer, A. Yariv, J. D. O'Brien, P. D. Dapkus, and I. Kim, "Two-Dimensional Photonic Band-Gap Defect Mode Laser", *Science* **284**, 1819-1821 (1999).
11. A. R. Cowan, and Jeff F. Young, "Mode Matching for Second Harmonic Generation in Photonic Crystal Waveguides", to appear in *Phys. Rev. B* on February 15, 2002.
12. E. Popov, and M. Neviere, "Surface-enhanced second-harmonic generation in nonlinear corrugated dielectrics: new theoretical approaches", *J. Opt. Soc. Am. B* **11**, 1555-1564 (1994).
13. P. Vincent, N. Paraire, M. Neviere, A. Koster, and R. Reinisch, "Gratings in nonlinear optics and optical bistability", *J. Opt. Soc. Am. B* **2**, 1106-1116 (1985).
14. Elsa Garmire, "Resonant Optical Nonlinearities in Semiconductors", *IEEE Journal on selected topics in Quantum Electronics* **6**, 1094-1110 (2000).
15. E. Centeno, and D. Felbacq, "Optical bistability in finite-size nonlinear bidimensional photonic crystals doped by a microcavity", *Phys. Rev. B* **62**, R7683-R7686 (2000).
16. G. Assanto, M. B. Marques, and G. I. Stegeman, "Grating coupling of light pulses into third-order nonlinear waveguides," *J. Opt. Soc. Am. B* **8**, 553-561 (1991).
17. C. Liao, G. I. Stegeman, C. T. Seaton, R. L. Shoemaker, and J. D. Velera, "Nonlinear distributed waveguide couplers," *J. Opt. Soc. Am. A* **2**, 590-594 (1985).
18. R. M. Fortenberry, G. Assanto, R. Moshrefzadeh, C. T. Seaton, and G. I. Stegeman, "Pulsed excitation of nonlinear distributed coupling into zinc oxide optical guides," *J. Opt. Soc. Am. B* **5**, 425-431 (1988).
19. M. Neviere, E. Popov, and R. Reinisch, "Electromagnetic resonances in linear and

- nonlinear optics: phenomenological study of grating behavior through the poles and zeros of the scattering operator,” J. Opt. Soc .Am . A **12**, 513-523 (1995).
20. P. Tran, “Photonic band-structure calculation of material possessing Kerr nonlinearity,” Phys. Rev B **52**, 10673-10676 (1995).
 21. V. Lousse, and J. P. Vigneron, “Self-consistent photonic band structure of dielectric superlattices containing nonlinear optical materials”, Phys. Rev. E **63**, 027602 (2001).
 22. A. Hache, and M. Bourgeois, “Ultrafast all-optical switching in a silicon-based photonic crystal,” Appl. Phys. Lett **77**, 4089-4091 (2000).
 23. S. V. Popov, Y. P. Svirko, and N. I. Zheludev, “ Susceptibility tensors for nonlinear optics,” (Institute of Physics Publishing, Bristol, 1995).
 24. A. A. Said, M. Sheik-bahae, D. J. Hagan, T. H. Wei, J. Wang, J. Young, and E. W. Van Stryland, “ Determination of bound-electron and free-carrier nonlinearities in ZnSe, GaAs, CdTe, and ZnTe,” J. Opt. Soc .Am . B **9**, 405-414 (1992).

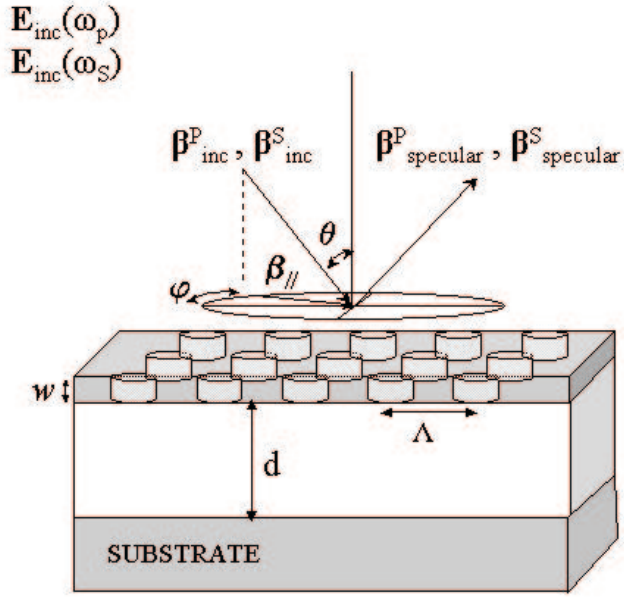


Fig. 1. Schematic representation of two-dimensional waveguide-based photonic crystal. Here we consider a square lattice of cylindrical holes on a pitch Λ , with radius r that completely penetrate the GaAs slab of thickness w . This porous core rests on a dielectric cladding layer of thickness d , that separates it from a GaAs substrate. Plane waves of arbitrary polarization are incident with in-plane wavevectors $\vec{\beta}_{||}$.

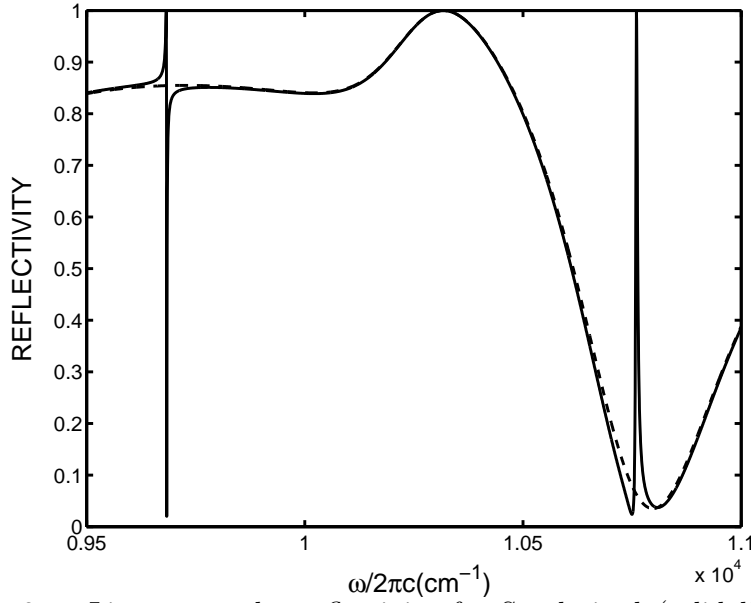


Fig. 2. Linear specular reflectivity for S-polarized (solid line) and P-polarized (dashed line) incident plane waves with in-plane wave vector $\beta_{//} = 0.01\beta_g$ oriented along the $\Gamma - X$ direction of the square lattice.

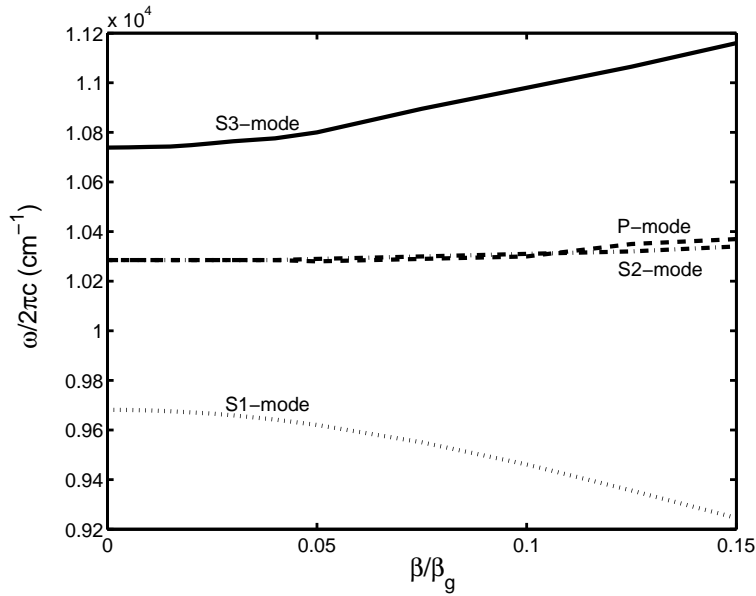


Fig. 3. Dispersion of the lowest lying four modes near zone-centre, as identified in Fig.(2). Each band has a different line-type that corresponds to those used in Fig.(5). These bands are labeled with increasing energy as s1,s2,p1 and s3.

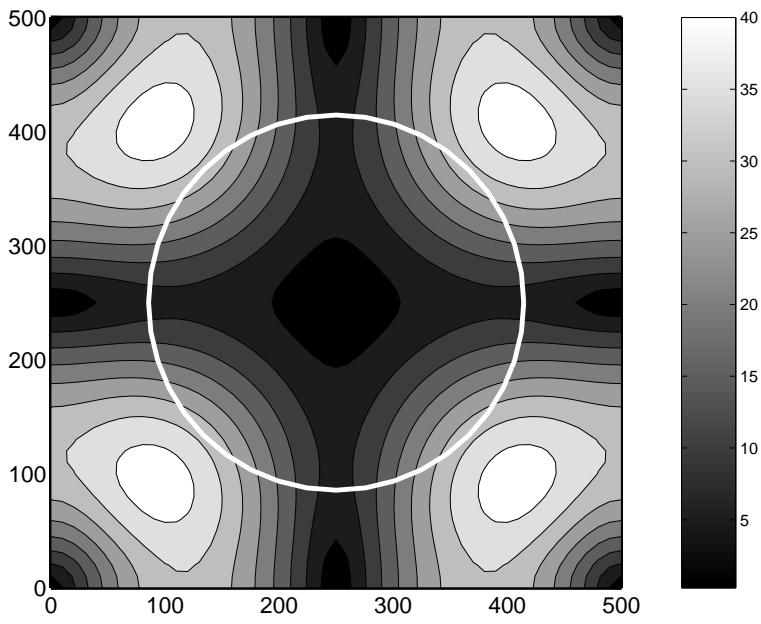


Fig.(4a)

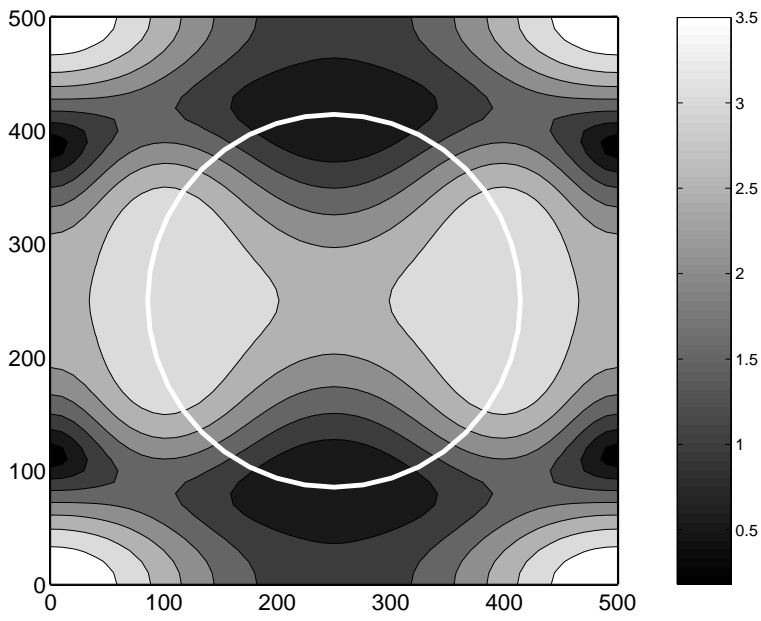


Fig.(4b)

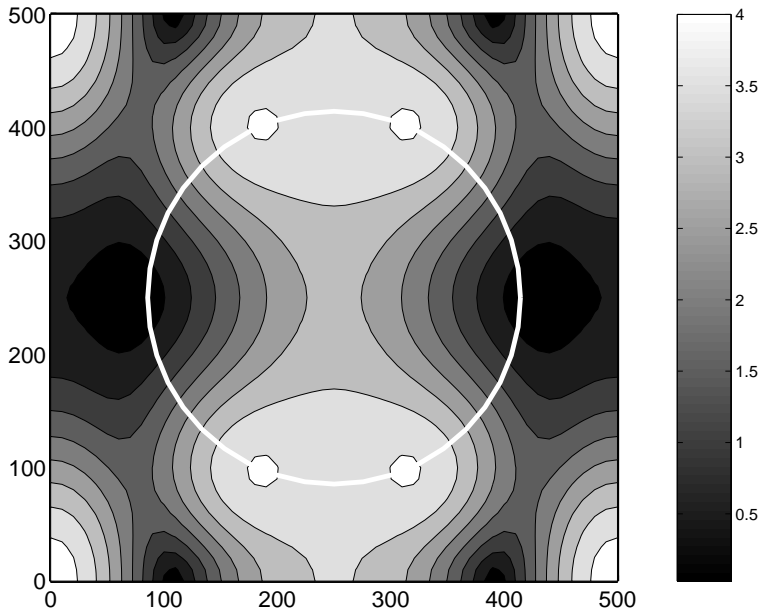


Fig.(4c)

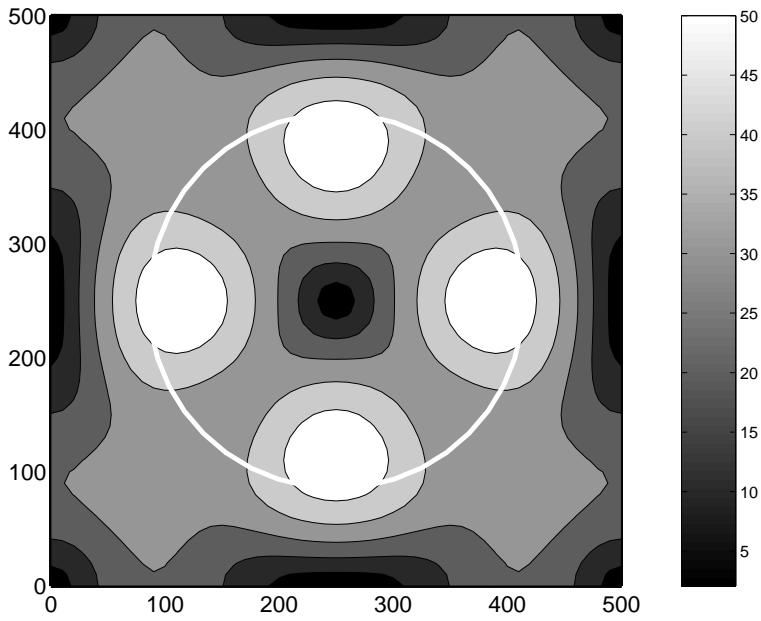


Fig.(4d)

Fig. 4. Real space plots of the magnitude of the total electric field within the unit cell for s1 (a), s2 (b), p1 (c), and s3 (d), all corresponding to the modes apparent in Fig.(2). The circle represents the perimeter of the air hole etched in the core layer. The horizontal and vertical scales are in units of nm, and the gray scales are arbitrary in an absolute sense, but consistent from plot to plot.

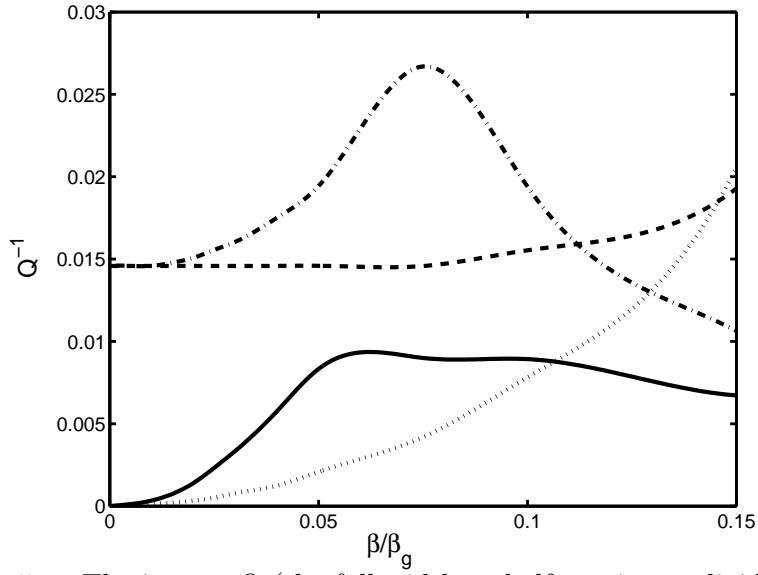


Fig. 5. The inverse Q (the full-width at half maximum divided by the centre frequency) of the same bands shown in Fig.(3) (the line types correspond).

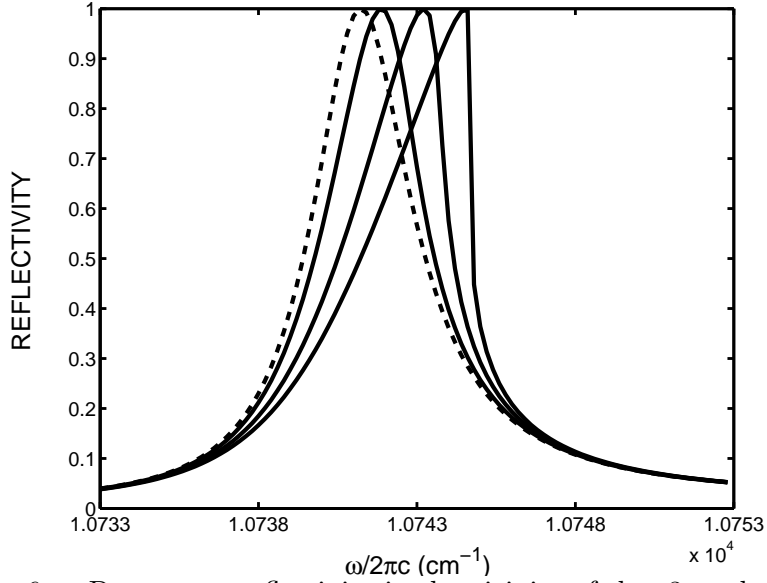


Fig. 6. Degenerate reflectivity in the vicinity of the s_3 mode in Fig.(2) for various incident field intensities; linear limit (dashed line), and progressively blue-shifted solid lines are for intensities of 765, 2342, and 3871 kW/cm^2 .

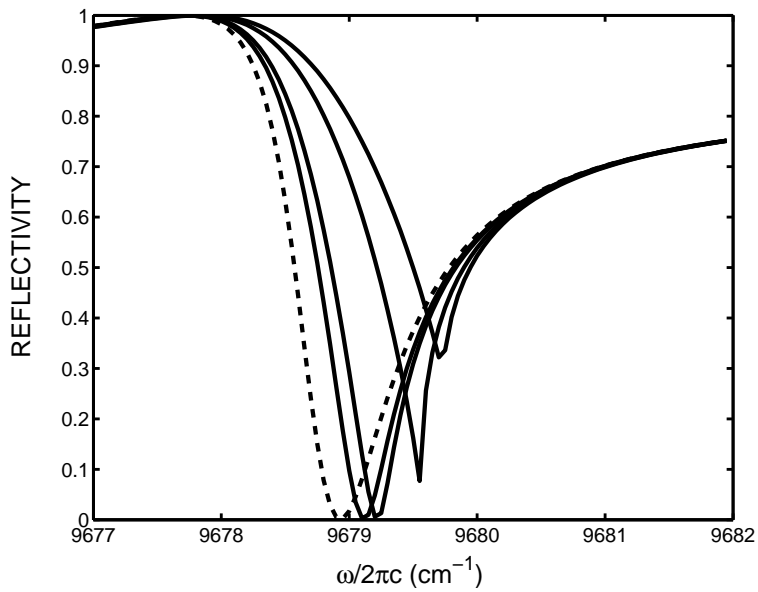


Fig. 7. Degenerate reflectivity in the vicinity of the s1 mode in Fig.(2) for various incident field intensities; linear limit (dashed line), and progressively blue-shifted solid lines are for intensities of 30, 48,107, and 155 kW/cm^2 .

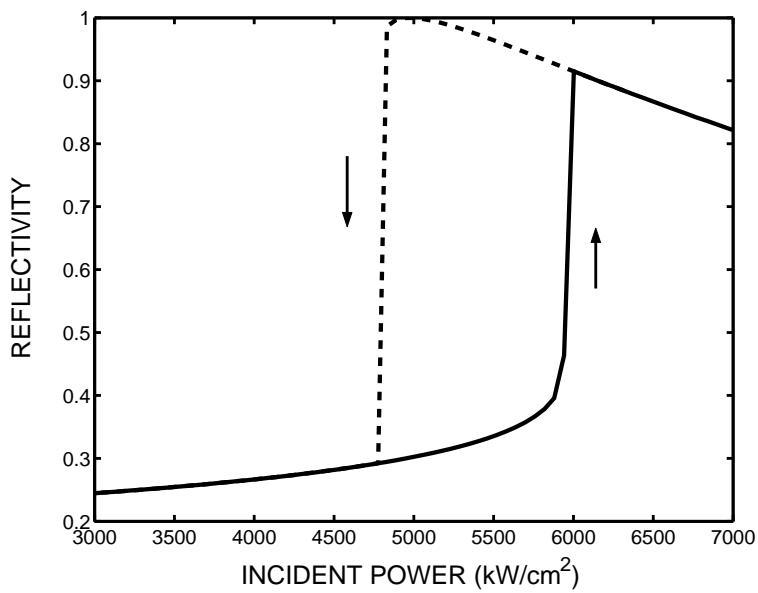


Fig. 8. Bistable behavior (degenerate) of reflectivity in the vicinity of the s3 resonance in Fig.(2).

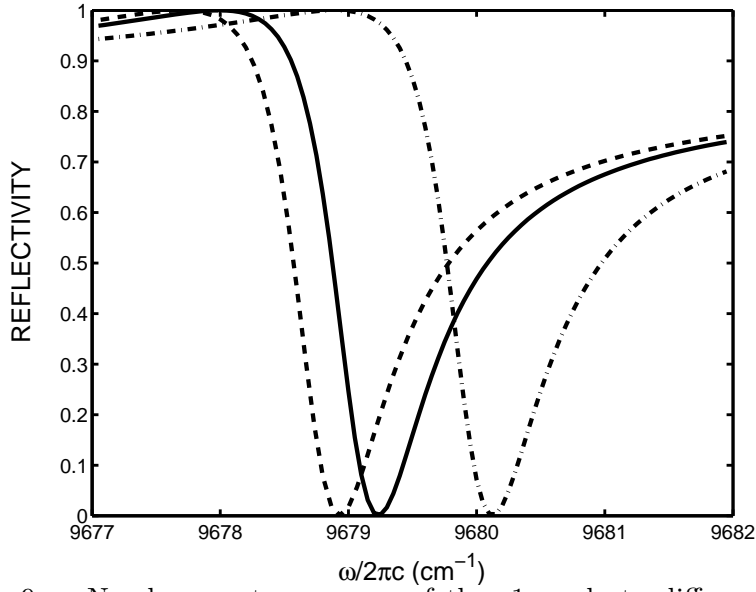


Fig. 9. Nondegenerate response of the s1 mode to different pump intensities with the pump frequency fixed at 10744cm^{-1} . The $\vec{\beta}_{//}$ is fixed at $0.01\beta_g\hat{x}$ for all pump and probe frequencies. Intensities of pump beams are 1720 (solid line) and 3058 (dash-dot line) kW/cm^2 . The dashed line represents the linear (low intensity limit) spectrum.

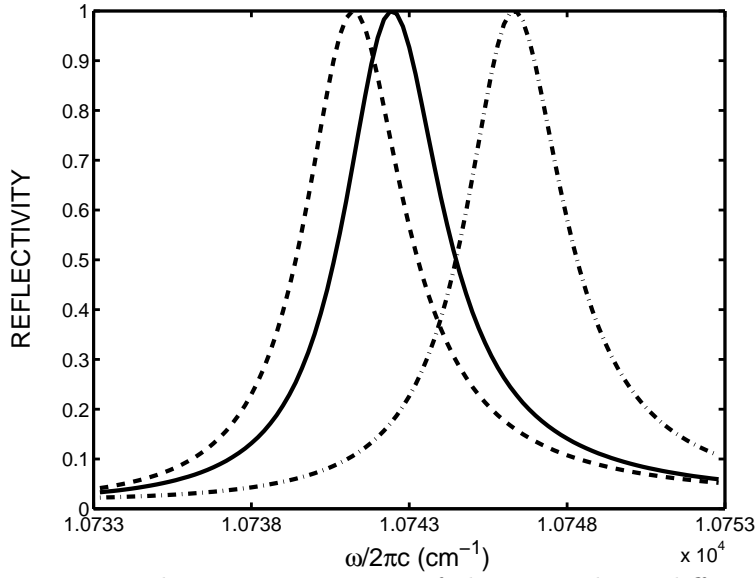


Fig. 10. Nondegenerate response of the s3 mode to different pump intensities with the pump frequency fixed at 10744cm^{-1} . The $\vec{\beta}_{//}$ is fixed at $0.01\beta_g\hat{x}$ for all pump and probe frequencies. Intensities of pump beams are 1720 (solid line) and 3058 (dash-dot line) kW/cm^2 . The dashed line represents the linear (low intensity limit) spectrum.